CrossMark

Influence of La^{3+} on structural, magnetic, dielectric, electrical and modulus spectroscopic characteristics of single phase CoFe$_{2-x}$La$_x$O$_4$ nanoparticles

Raghvendra Singh Yadav[1] · Ivo Kuřitka[1] · Jarmila Vilcakova[1] · Jaromir Havlica[2] ·
Lukas Kalina[2] · Pavel Urbánek[1] · Michal Machovsky[1] · Milan Masař[1] · Martin Holek[1]

Abstract In this work, we have studied the influence of La^{3+} substitution on structural, magnetic, dielectric, electrical and modulus spectroscopic characteristics of cobalt ferrite nanoparticles synthesized by starch-assisted sol–gel combustion method. The powder X-ray diffraction analysis confirms the formation of single-phase CoFe$_{2-x}$La$_x$O$_4$ (x = 0.00, 0.05, 0.10, 0.15, 0.20) spinel ferrite nanoparticles. Raman spectroscopy study also reveals the formation of single phase spinel ferrite crystal structure. The morphological feature of synthesized ferrite nanoparticle was observed by scanning electron microscopy that demonstrate formation of spherical nanoparticles with grain size 10–50 nm. The presence of constituent's, i.e., Co, Fe and La were authenticated by energy dispersive X-ray analysis. The magnetic parameters are measured by employing vibrating sample magnetometer. The saturation magnetization decreases with La^{3+} substitution, whereas coercivity shows anomalous behaviour. Cation redistribution in spinel ferrite nanoparticles are confirmed by X-ray photoelectron spectroscopy. The variation of dielectric constant (ϵ', ϵ''), loss tangent (tanδ), ac conductivity (σ), electric modulus (M′, M″) and impedance (Z′, Z″) as a function of La^{3+} ion concentration and frequency has been investigated. The dielectric constant and ac conductivity increases with increase of La^{3+} substitution, whereas dielectric loss tangent exhibits anomalous behaviour. The modulus spectra reveal two semicircles associated with grain and grain boundary effects. The cole–cole plots in modulus formalism show that the electrical characteristics contribute from both the grains and grain boundaries. Modulus spectra suggest that the distribution of relaxation times and conduction mechanism are influenced by La^{3+} ion substitution in cobalt ferrite nanoparticles.

1 Introduction

Recently, spinel ferrite nanoparticles have attracted considerable research interest due to their wide range of applications in drug delivery, as contrast agent, in hyperthermia, magnetic recording, microwave absorption, multilayer chip inductors, transformer cores, rod antennas, catalysis, gas sensor, energy storage devices, high-performances electrodes for lithium ion batteries, etc. [1–10]. Among the spinel ferrite, cobalt ferrite is hard magnetic material, which has a cubic spinel structure with excellent magnetic, electrical property and chemical stability, has been extensively used for various technological applications [11, 12]. A remarkable physical properties are observed in doped complex inorganic nanostructures by several researchers [13–16]. The substitution of rare-earth ions in spinel ferrite nanoparticles has emerged as a promising strategy to tune the magnetic, dielectric and electrical properties [17, 18]. The magnetic, dielectric and electrical properties of rare-earth ion substituted spinel ferrite nanoparticles depend on rare-earth ion, cation distribution, grain size, synthesis method, etc [19, 20].

Different synthesis techniques such as co-precipitation, sol–gel, micro-emulsion, hydrothermal, solvothermal, combustion method have been employed to synthesize rare-earth substituted spinel ferrite nanoparticles [21, 22].

✉ Raghvendra Singh Yadav
  yadav@cps.utb.cz; raghvendra.nac@gmail.com

[1] Centre of Polymer Systems, University Institute, Tomas Bata University in Zlín, Trida Tomase Bati 5678, 760 01 Zlín, Czech Republic

[2] Materials Research Centre, Brno University of Technology, Purkyňova 464/118, 61200 Brno, Czech Republic

Solution combustion method is an effective energy saving and low cost method for production of rare-earth ion substituted spinel ferrite nanoparticles [23]. R. C. Kambale et al. [24] found that combustion technique is more advantageous than the others for the synthesis of rare-earth ion substituted single phase spinel ferrite nanoparticles. The influence of La^{3+} ion substitution in cobalt ferrite synthesized by different synthesis method, have been studied by different researchers. R. Indhrajothi et al. [25] reported La^{3+} substituted cobalt ferrite nanoparticles prepared by citric acid, urea, and glycerol assisted foam combustion process. This research group observed that the presence of La^{3+} ion improved the oxidation reaction of Fe and Co element and capacity retention as compared to pristine cobalt ferrite anode material. However, the presence of La^{3+} reduced the electrical conductivity of cobalt ferrite. S. F. Mansour et al. [26] observed influence of La doping and synthesis methods on the magnetic properties of cobalt ferrite nanoparticles. Nanocrystals of La doped $CoFe_2O_4$ were synthesized using three different techniques: flash auto-combustion, citrate–nitrate and the standard ceramic technique. This research group noticed that the citrate method displayed superior saturation magnetization values amongst all techniques. The coercivity was found to exhibit largest values for the citrate method and then the flash while smallest values were associated with ceramic technique. L. Kumar et al. [27] studied the effect of La^{3+} substitution on the magnetic property of cobalt ferrite synthesized by citrate precursor method. The saturation magnetization, coercivity and magnetocrystalline anisotropy constants were found to decrease with increase of La^{3+} ion concentration. P. Kumar et al. [28] reported the influence of La^{3+} doping on the electric, dielectric and magnetic properties of cobalt ferrite processed by co-precipitation technique. This research group noticed that incorporation of La^{3+} increased the dc resistivity of cobalt ferrite, however, saturation magnetization was decreased. K. K. Bharathi et al. [29] investigated coexistence of spin glass behaviour and long range ferrimagnetic ordering in La doped cobalt ferrite. We feel that the earlier studies on physical properties of La^{3+} doped cobalt ferrite nanoparticles has not been well studied in detailed on structural characteristics and its physical property with impedance and modulus formalism. Therefore, our research group has focused on detailed investigation of structural, cation distribution, magnetic, dielectric, electrical, impedance and modulus spectroscopy characteristics of La^{3+} doped cobalt ferrite nanoparticles.

In present study, we report the starch-assisted sol–gel combustion synthesis of La^{3+} substituted cobalt ferrite nanoparticles. Further, the variation in structural, cation distribution, magnetic, dielectric, electrical, impedance and modulus spectroscopic characteristics of $CoFe_2O_4$ nanoparticles on La^{3+} ion substitution in place of Fe^{3+}, are

investigated in details. The substitution of La^{3+} in cobalt ferrite nanoparticles significantly influences the magnetic, dielectric and electrical properties.

2 Experimental section

2.1 Synthesis

A series of La^{3+} doped cobalt ferrite nanoparticles with a formula $CoFe_{2-x}La_xO_4$ (x = 0.0, 0.05, 0.10, 0.15, 0.20) was synthesized by starch-assisted sol–gel combustion method. Analytical grade cobalt nitrate ($Co(NO_3)_2 \cdot 6H_2O$), iron nitrate ($Fe(NO_3)_3 \cdot 9H_2O$), lanthanum nitrate ($La(NO_3)_3 \cdot 6H_2O$) were used as starting materials. These chemicals were purchased from Alfa Aesar GmbH & Co. KG, Germany. The starch soluble ($C_6H_{10}O_5)_n$ (from potatoes) was used as fuel and was purchased from Lach-Ner, Czech Republic. The stoichiometric amount of cobalt nitrate ($Co(NO_3)_2 \cdot 6H_2O$), iron nitrate ($Fe(NO_3)_3 \cdot 9H_2O$) and lanthanum nitrate ($La(NO_3)_3 \cdot 6H_2O$) were dissolved in deionized water needed to obtain a clear solution. The molar ratio of cobalt nitrate to iron nitrate and lanthanum nitrate was 1:2. An aqueous solution of starch was mixed with above prepared metal-nitrate aqueous solution. This mixed aqueous solution was put on a hot plate with continuous stirring at 110 °C. After evaporation few minutes, the solution starts to formed a very viscous brown gel. This formed gel was heated to 350 °C to initiate a self-sustaining combustion reaction. The obtained combusted powders were hand-crushed with a pestle for following structural and physical property characterization.

2.2 Characterization techniques

Powder X-ray diffraction pattern of synthesized series of $CoFe_{2-x}La_xO_4$ (x = 0.0, 0.05, 0.10, 0.15, 0.20) nanoparticles were recorded on Rigaku MiniFlex 600 X-ray Spectrometer with a filtered cobalt source. Raman spectra of synthesized ferrite nanoparticles were measured by using Dispersive Raman microscope Nicolet DXR equipped with excitation laser and excitation wavelength 780 nm. The morphology of La^{3+} substituted cobalt ferrite nanoparticle was examined by scanning electron microscope Nova NanoSEM450 (FEI company). The magnetic properties of synthesized $CoFe_{2-x}La_xO_4$ (x = 0.0, 0.05, 0.10, 0.15, 0.20) nanoparticles were investigated using a vibrating sample magnetometer (VSM 7407, Lake Shore) at room temperature. The dielectric properties such as dielectric constant and dielectric loss tangent were measured using a Broadband Dielectric Impedance Analyzer Concept 40 (Novocontrol, Germany). The sample dimension for dielectric and electrical property measurement was 20 mm
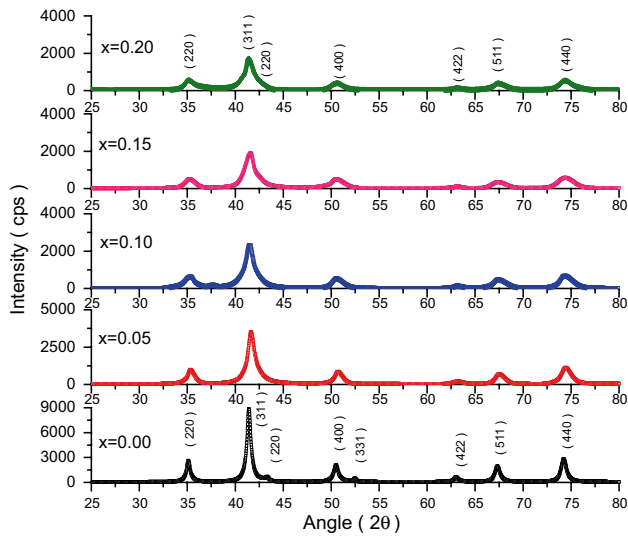
Fig. 1 XRD pattern for $CoFe_{2-x}La_xO_4$ (x = 0.00, 0.05, 0.10, 0.15, 0.20) nanoparticles synthesized by starch assisted sol–gel combustion method

Table 1 Influence of La^{3+} ion on crystallite size (D), lattice parameter (a), X-ray density (d_x) and hopping lengths (d_A and d_B) for $CoFe_{2-x}La_xO_4$ (x = 0, 0.05, 0.10, 0.15, 0.20) nanoparticles synthesized by starch-assisted sol–gel combustion method

x	D (nm)	a (Å)	d_x (g cm^{-3})	d_A(Å)	d_B (Å)
0.00	21	8.3886	5.28	3.6323	2.9654
0.05	14	8.3463	5.45	3.6139	2.9504
0.10	11	8.3539	5.54	3.6172	2.9531
0.15	9	8.3693	5.59	3.6239	2.9585
0.20	8	8.3964	5.64	3.6356	2.9681

in diameter and 0.5 mm in thickness. Further, the modulus and impedance spectra of synthesized La^{3+} substituted cobalt ferrite nanoparticles was determined using a standard sample cell BDS 1200 employing RC model.

3 Result and discussion

3.1 Structural study

The identification of crystal phase of $CoFe_{2-x}La_xO_4$ nanoparticles was performed by utilizing X-ray Diffraction (XRD) characterization technique. The typical XRD pattern of synthesized $CoFe_{2-x}La_xO_4$ (x = 0, 0.05, 0.10, 0.15, 0.20) nanoparticles is shown in Fig. 1. The observed diffraction peaks matched well with standard $CoFe_2O_4$ (PDF Card No.: 00-002-1045) for X-rays (1.78897 Å for Co K_α). It can be noticed from Fig. 1 that the diffraction peak intensity decreases with increase of La concentration because of

decrease in crystallite size. The crystallite size of synthesized $CoFe_{2-x}La_xO_4$ (x = 0, 0.05, 0.10, 0.15, 0.20) nanoparticles was calculated by using Scherrer equation [30]:

$$D = 0.9\, \lambda_{Co}/B\, Cos\theta$$

where D is the crystallite size, B is the half maximum line width, λ is the wavelength of radiation used (1.78897 Å for Co K_α), and θ is the angle of diffraction. The calculated average crystallite size of $CoFe_{2-x}La_xO_4$ (x = 0, 0.05, 0.10, 0.15, 0.20) nanoparticles is tabulated in Table 1. The decrease in crystallite size from 21 to 8 nm with increase of La concentration can be noticed from Table 1. The La^{3+} ion (1.06 Å) has higher ionic radii in comparison to Fe^{3+} ion (0.67 Å), therefore, it is not easy to replace Fe^{3+} ion in $CoFe_2O_4$ spinel ferrite nanoparticles. Consequently, few La^{3+} ions may reside on the grain boundaries. These higher ionic radii La^{3+} ions produce pressure on the grain boundaries and hinders the growth of grains, therefore, crystallite size of La doped cobalt ferrite nanoparticles decreases with increase of La content [31, 32]. The lattice parameter of synthesized $CoFe_{2-x}La_xO_4$ (x = 0, 0.05, 0.10, 0.15, 0.20) nanoparticles were calculated using the following relation [33]:

$$a = \frac{\lambda_{Co}}{2} \times \sqrt{((h^2 + k^2 + l^2)/Sin^2\theta)}$$

where a is the lattice constant, λ is the wavelength (1.78897 Å for Co K_α), h, k and l are Miller indices, and θ is the position of X-ray diffraction peak.

The lattice parameter was found to decrease with addition of La ions and it was further increased with increase of La ions in $CoFe_2O_4$ spinel ferrite nanoparticles, as tabulated in Table 1. The variation in lattice parameter of La^{3+} ion in cobalt ferrite nanoparticles depends on three factors (i) higher ionic radii tend to increase lattice parameter, (ii) created strain due to La^{3+} ion substitution tries to decrease, and (iii) cation redistribution with substitution of La^{3+} ion [34]. The observed decrease in lattice parameter from 8.3886 Å (x = 0.00) to 8.3463 Å (x = 0.05) with La^{3+} substitution seems due to created strain and further increase in lattice parameter from 8.3463 Å (x = 0.05) to 8.3964 Å (x = 0.20) is related with cation redistribution and higher ionic radii of La^{3+} ion.

The X-ray density of synthesized $CoFe_{2-x}La_xO_4$ (x = 0, 0.05, 0.10, 0.15, 0.20) nanoparticles was determined using the following relation [35]:

$$d_x = \frac{8M}{Na^3}$$

where, 'M' is the molecular mass, 'N' is Avogadro's number and 'a^3' is the volume of the cubic unit cell. The calculated value of X-ray density of synthesized $CoFe_{2-x}La_xO_4$ (x = 0, 0.05, 0.10, 0.15, 0.20) nanoparticles is tabulated in Table 1. It was found that the X-ray density increases

from 5.28 g cm^{-3} (x = 0.00) to 5.64 g cm^{-3} (x = 0.20) with increase of La ion concentration in $CoFe_2O_4$ nanoparticles. The increase in the value of X-ray density with increase of La ion substitution is due to larger mass of ions.

The hopping length between the magnetic ions in the tetrahedral (A) and octahedral site (B) for $CoFe_{2-x}La_xO_4$ (x = 0, 0.05, 0.10, 0.15, 0.20) nanoparticles is evaluated using following relations [36]:

$$d_A = \left(\frac{a}{4}\right)\sqrt{3}$$

$$d_B = \left(\frac{a}{4}\right)\sqrt{2}$$

where, d_A and d_B are hopping length for tetrahedral site and octahedral site, respectively. The evaluated value of d_A and d_B are tabulated in Table 1. It is noticeable that hopping length decreases with substitution of La^{3+} ion, which is associated with replacement of Fe^{3+} ions by the relative number of La^{3+} ions at octahedral (B) site in cobalt ferrite nanoparticles. Further, with increase of further substitution of La^{3+}, hopping length increases which is associated with cation redistribution between tetrahedral (A) and octahedral (B) site. The X-ray parameters for cubic spinel structure, viz. A-site radii (r_A), B-site radii (r_B), tetrahedral and octahedral bond length d_{Ax} and d_{Bx}, tetrahedral edge, shared and unshared octahedral edge (d_{AxE}, d_{BxE}, d_{BxEU}) were calculated using the experimental values of lattice parameter 'a', oxygen positional parameter 'u' (u = 0.381 Å) and oxygen ion radius R_o and substituting these values into the following equation [37]:

$$r_A = (u - 0.25)a\sqrt{3} - R_o$$

$$r_B = (0.625 - u)a - R_o$$

$$d_{Ax} = a\sqrt{3}(u - 1/4)$$

$$d_{Bx} = a[3u^2 - (11/4)u + (43/64)]^{1/2}$$

$$d_{AxE} = a\sqrt{2}(2u - 1/2)$$

$$d_{BxE} = a\sqrt{2}(1 - 2u)$$

$$d_{BxEU} = a[4u^2 - 3u + (11/16)]^{1/2}$$

The calculated value of r_A, r_B, d_{Ax}, d_{Bx}, d_{AxE}, d_{BxE}, d_{BxEU} is tabulated in Table 2. From Table 2, it is noticeable that A-site radii (r_A), B-site radii (r_B), tetrahedral and octahedral bond length d_{Ax} and d_{Bx}, tetrahedral edge, shared and unshared octahedral edge (d_{AxE}, d_{BxE}, d_{BxEU}) decreases to some extent with La^{3+} ion substitution due to higher ionic radii of La^{3+} ion as compared Fe^{3+} ion and created strain with La^{3+} substitution. Furthermore, these structural parameters are increased with further substitution of La^{3+} ions, which is related to cation redistribution at A-site and B-site in cobalt ferrite nanoparticles.

3.2 Raman spectroscopy

Raman spectroscopy is a powerful characterization technique to investigate crystal structure of spinel ferrite. Figure 2 shows the Raman spectra for $CoFe_{2-x}La_xO_4$ (x = 0.00, 0.05, 0.10, 0.15, 0.20) nanoparticles synthesized by starch-assisted sol–gel combustion method. The group theory analysis of the lattice vibrations in the *Fd3m* structure with eight formula units per unit cell predicts five Raman active phonon modes, $A_{1g} + E_g + 3T_{2g}$ [38]. Here, A, E and T are for one dimensional, two dimensional and three dimensional representations, respectively. These five Raman modes are associated with the motion of oxygen anions and cations at both tetrahedral and octahedral sites in spinel ferrite. The A_{1g} Raman mode involves mainly the motion of oxygen anions and the remaining other four Raman modes ($E_g + 3T_{2g}$) is related to motion of both oxygen anions and cations [39]. The presence of five Raman modes in Fig. 2, indicate formation of single phase cubic spinel structure. The strong Raman mode around 670 cm^{-1} corresponds to A_{1g} and can be assigned to symmetric stretching of oxygen atoms along metal–oxygen and Fe-O bonds at tetrahedral sites. The Raman mode $T_{2g}(3)$ around 590 cm^{-1} corresponds to asymmetric bending of oxygen and the Raman

Table 2 Structural parameters: tetrahedral (A)-site radii (r_A), octahedral (B)-site radii (r_B), tetrahedral and octahedral bond length d_{Ax} and d_{Bx}, tetrahedral edge, shared and unshared octahedral edge (d_{AxE}, d_{BxE}, d_{BxEU}) for $CoFe_{2-x}La_xO_4$ (x = 0, 0.05, 0.10, 0.15, 0.20) nanoparticles synthesized by starch-assisted sol–gel combustion method

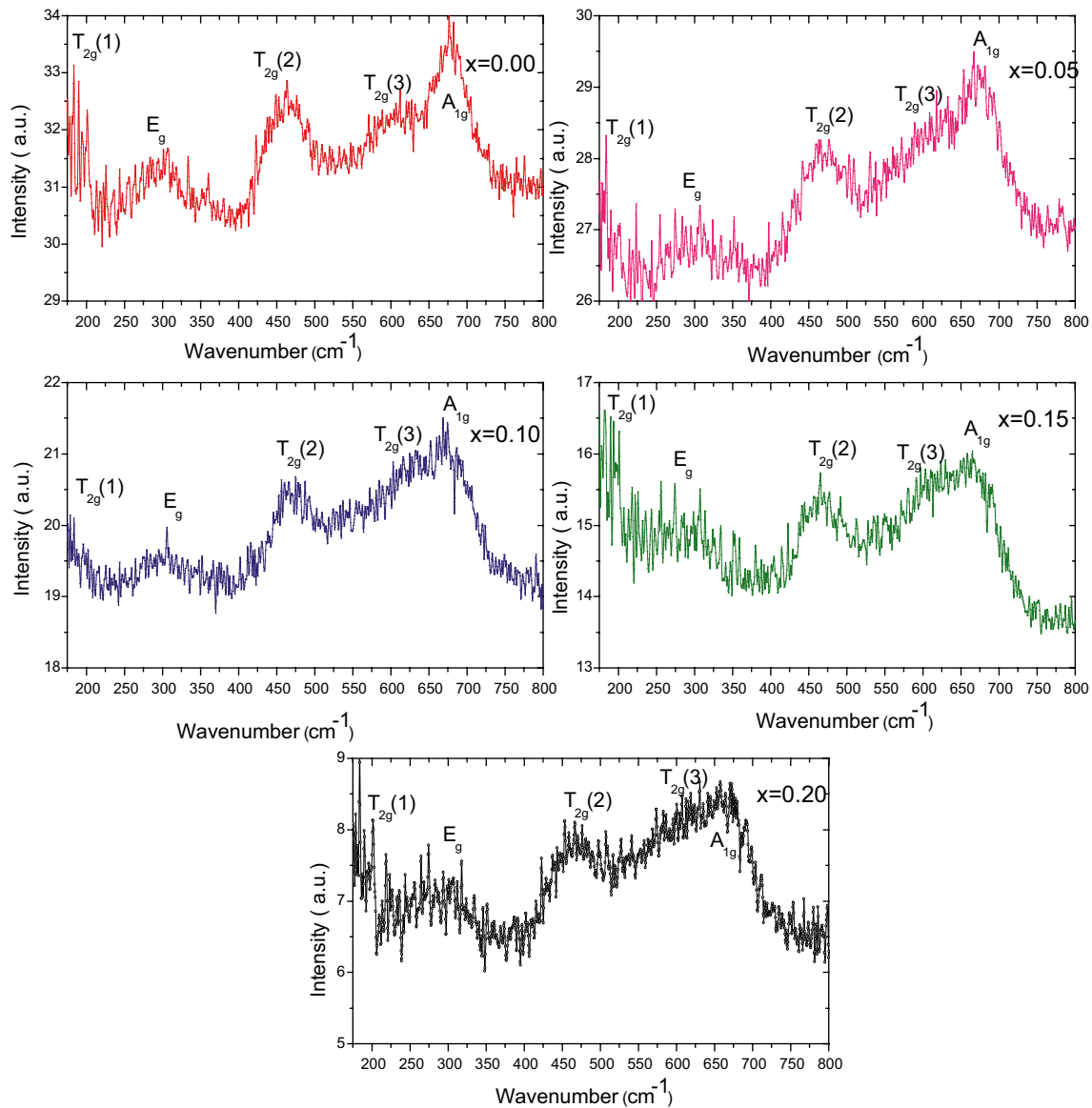| x	r_A (Å)	r_B (Å)	d_{Ax} (Å)	d_{Bx} (Å)	d_{AxE} (Å)	d_{BxE} (Å)	d_{BxEU} (Å)
0.00	0.5833	0.7268	1.9033	2.0479	3.1077	2.8230	2.9675
0.05	0.5737	0.7165	1.8937	2.0376	3.0920	2.8088	2.9525
0.10	0.5754	0.7184	1.8954	2.0395	3.0948	2.8114	2.9552
0.15	0.5789	0.7221	1.8989	2.0433	3.1006	2.8165	2.9607
0.20	0.5851	0.7287	1.9051	2.0498	3.1105	2.8256	2.9703

Fig. 2 Raman spectra of $CoFe_{2-x}La_xO_4$ (x = 0.00, 0.05, 0.10, 0.15, 0.20) nanoparticles synthesized by starch-assisted sol–gel combustion method

modes $T_{2g}(2)$ around 460 cm^{-1} corresponds to asymmetric stretching of metal–oxygen and Fe-O at octahedral site. The Raman mode $T_{2g}(1)$ around 190 cm^{-1} corresponds to translational motion of tetrahedron. The Raman mode E_g around 300 cm^{-1} is associated with symmetric bending of oxygen with respect to metal ion [40]. The variation in Raman peak position and Raman intensity is associated with cation redistribution and crystallite size of $CoFe_{2-x}La_xO_4$ (x = 0.00, 0.05, 0.10, 0.15, 0.20) nanoparticles.

3.3 Morphology and EDX study

Figure 3 shows the scanning electron microscopy image of $CoFe_{2-x}La_xO_4$ (x = 0.00, 0.15 and 0.20) nanoparticles synthesized by starch-assisted sol–gel combustion method. From Fig. 3, it can be notice that un-doped and La doped cobalt ferrite nanoparticles were spherical in morphology with little agglomeration. The ferrite nanoparticles were with grain size distribution 20–80 nm for x = 0.0, 10–60 nm for x = 0.15 and 5–50 nm for x = 0.20, as shown in Fig. 3a–c. Further study of energy dispersive X-ray
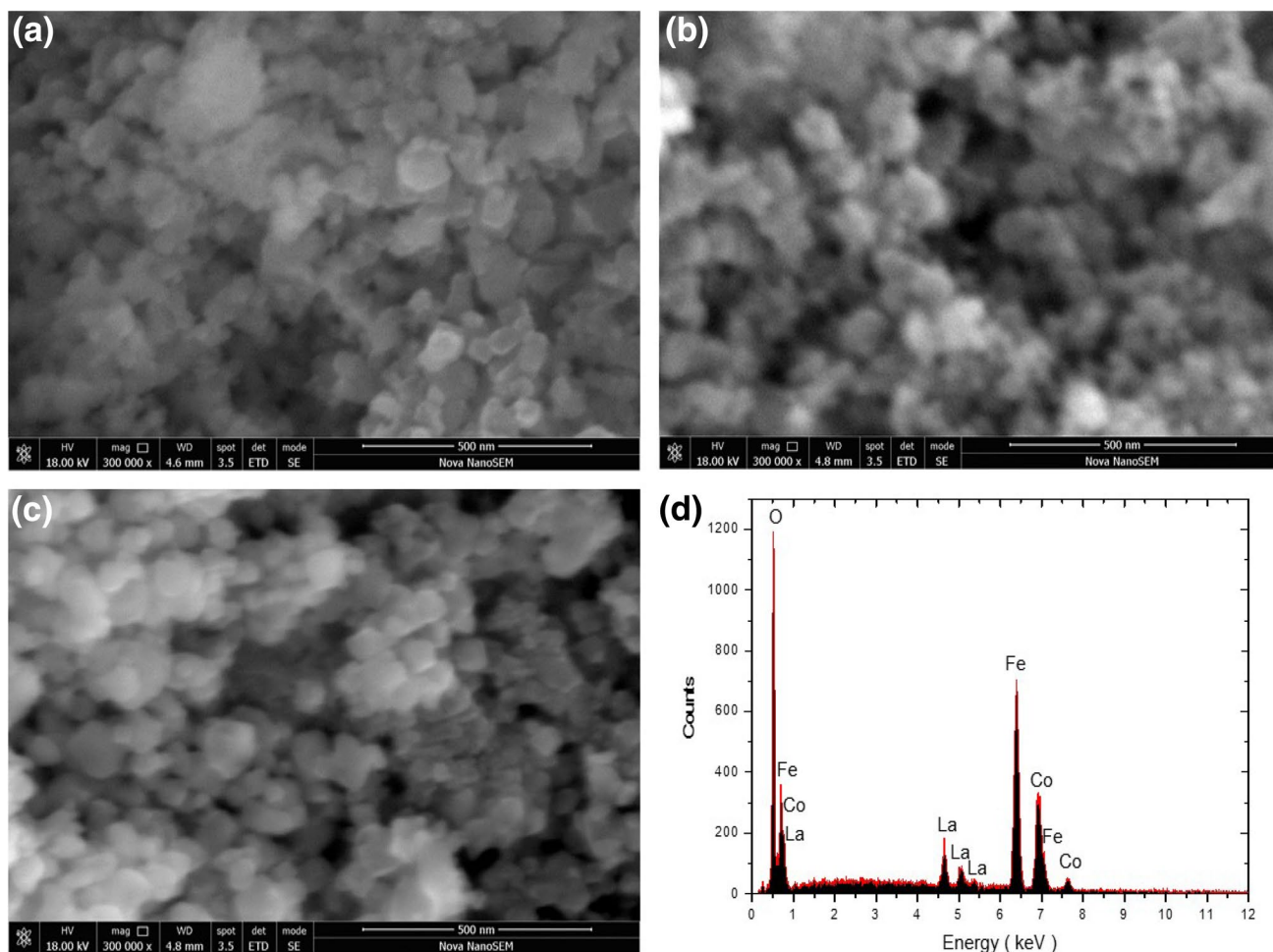
Fig. 3 Scanning electron microscopy image for $CoFe_{2-x}La_xO_4$ nanoparticles. **a** x = 0.0. **b** x = 0.15. **c** x = 0.20. **d** EDX spectrum of $CoFe_{2-x}La_xO_4$ nanoparticles for x = 0.20

spectra of cobalt ferrite nanoparticles (x = 0.20) confirms that La^{3+} ions exist in cobalt ferrite nanoparticles, as shown in Fig. 3d.

3.4 XPS study and cation distribution

The oxidation state of Co and Fe and their presence at tetrahedral and octahedral site in spinel ferrite lattice are examined by X-ray photoelectron spectroscopy. Co 2p and Fe 2p core level XPS spectra for $CoFe_{2-x}La_xO_4$ (x = 0.10 and 0.20) nanoparticles are shown in Fig. 4. These spectra were fitted with combined Gaussian–Lorentzian function. For $CoFe_{2-x}La_xO_4$ (x = 0.10) nanoparticles, in the Co 2p spectrum (Fig. 4a), the binding energy (B.E.) peak at 779.9 and 785.7 eV are corresponding to Co $2p_{3/2}$ and its shake-up satellite peak, respectively; however, another two B.E. peaks at 795.4 and 802.6 eV is associated to Co $2p_{1/2}$ and its shake-up satellite peak, respectively. The existence of Co $2p_{3/2}$ shakeup satellite peak indicate the presence of

Co^{2+} oxidation states in $CoFe_{2-x}La_xO_4$ (x = 0.10) nanoparticles [41]. The asymmetric nature of main B.E. peak Co $2p_{3/2}$ is associated with its distribution between tetrahedral and octahedral site. After fitting, the evaluated value of distribution of Co^{2+} at tetrahedral and octahedral site is tabulated in Table 3. Similar results can also be noticed for $CoFe_{2-x}La_xO_4$ (x = 0.20) nanoparticles in the Co 2p spectrum (Fig. 4b) and distribution of cation at different sites are tabulated in Table 3. Further, Fe 2p core level spectra as shown in Fig. 4c for $CoFe_{2-x}La_xO_4$ (x = 0.10) nanoparticles and in Fig. 4d for $CoFe_{2-x}La_xO_4$ (x = 0.20) nanoparticles suggest the existence of Fe^{3+} oxidation state [42]. These Fe^{3+} ions are also distributed at tetrahedral and octahedral site. The evaluated value of distribution of Fe^{3+} ions at different sites for $CoFe_{2-x}La_xO_4$ (x = 0.10 and 0.20) nanoparticles is tabulated in Table 3. From Table 3, it is noticeable that Fe^{3+} ions at tetrahedral and octahedral site was redistributed with further addition of La ion substitution in cobalt ferrite nanoparticles.
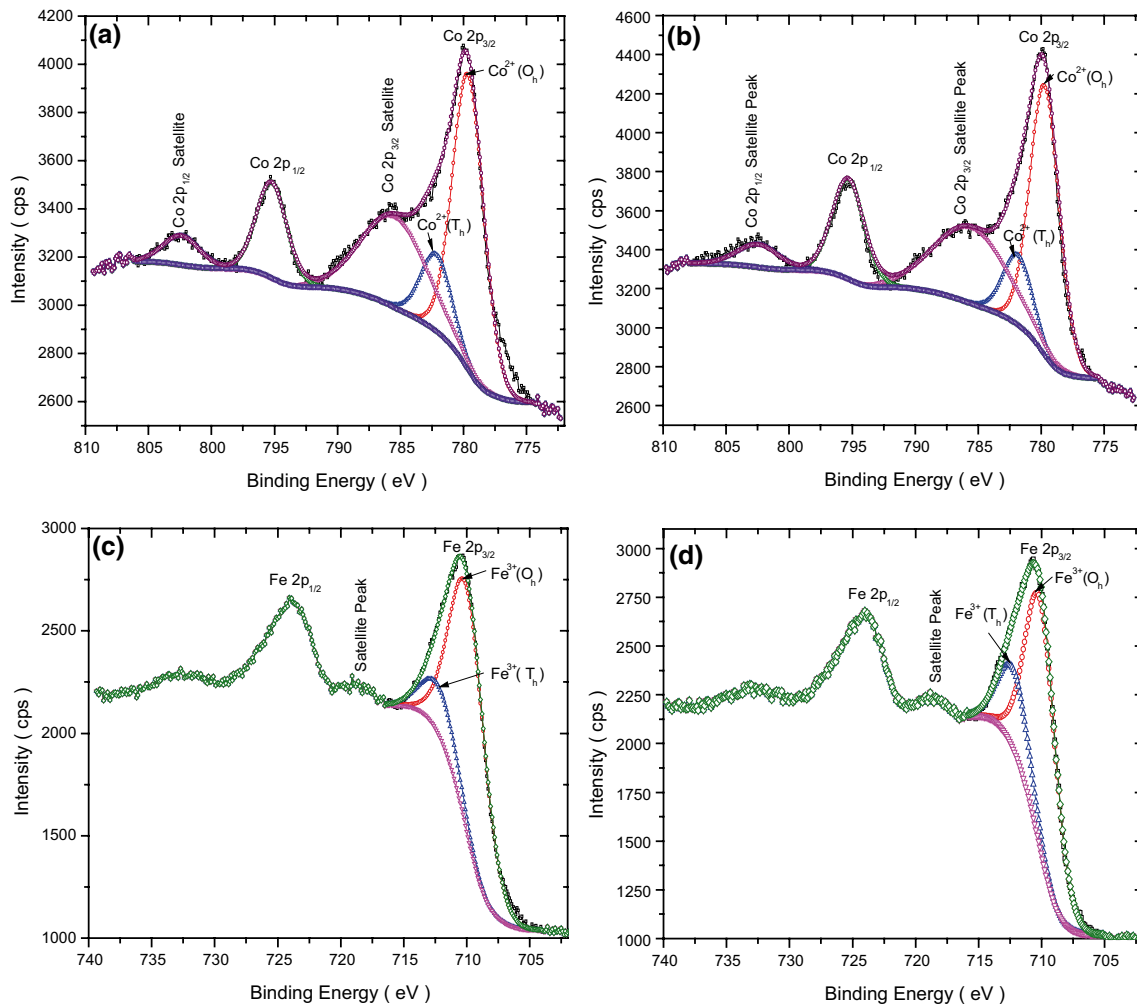
Fig. 4 X-ray photoelectron spectra of **a** Co 2p region for x = 0.10 and **b** Co 2p region for x = 0.20; and **c** Fe 2p region for x = 0.10 and **d** Fe 2p region for x = 0.20 of $CoFe_{2-x}La_xO_4$ nanoparticles synthesized by starch-assisted sol–gel combustion method

Table 3 XPS results: binding energy (B.E.), assignment of peak, atomic percentage for $CoFe_{2-x}La_xO_4$ (x = 0.10 and 0.20) nanoparticles

Sample	Spectrum	B.E. (eV)	Assignment	Atomic percentage (%)
$CoFe_{2-x}La_xO_4$ (x = 0.10)	Co 2p$_{3/2}$	779.6	Octahedral Co^{2+}	79
		782.2	Tetrahedral Co^{2+}	21
	Fe 2p$_{3/2}$	709.9	Octahedral Fe^{3+}	84
		712.7	Tetrahedral Fe^{3+}	16
$CoFe_{2-x}La_xO_4$ (x = 0.20)	Co 2p$_{3/2}$	779.7	Octahedral Co^{2+}	79
		781.8	Tetrahedral Co^{2+}	21
	Fe 2p$_{3/2}$	710.1	Octahedral Fe^{3+}	76
		712.2	Tetrahedral Fe^{3+}	24

3.5 Magnetic property

The magnetic properties of spinel ferrite magnetic nanoparticles depend upon cation distribution, crystallite size, crystallinity, chemical composition and synthesis technique, etc. The magnetic property of synthesized $CoFe_{2-x}La_xO_4$ (x = 0.0, 0.05, 0.10, 0.15, 0.20) nanoparticles were investigated by using vibrating sample magnetometer (VSM) at room temperature with an applied field 10 kOe. The magnetic hysteresis loops of $CoFe_{2-x}La_xO_4$ (x = 0.0, 0.05, 0.10, 0.15, 0.20) nanoparticles obtained by VSM at room temperature are shown in Fig. 5 and the magnetic parameters are tabulated in Table 4. It can be noticed from magnetic hysteresis loops of synthesized $CoFe_{2-x}La_xO_4$ (x = 0.0, 0.05, 0.10, 0.15, 0.20) nanoparticles that the pure and La^{3+} doped $CoFe_2O_4$ nanoparticles exhibit ferromagnetic behaviour

Fig. 5 Hysteresis curves of $CoFe_{2-x}La_xO_4$ (x = 0.00, 0.05, 0.10, 0.15, 0.20) nanoparticles synthesized by starch-assisted sol–gel combustion method and *inset* is enlarge view of hysteresis curves
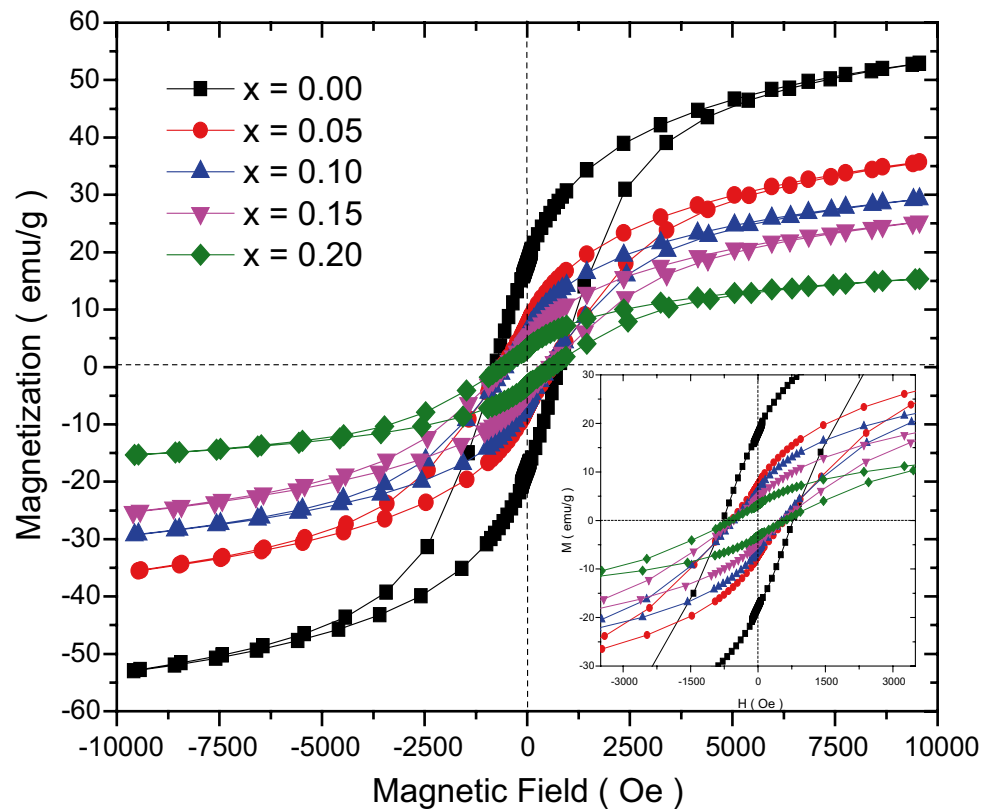

Table 4 Magnetic parameters: saturation magnetization (M_s), coercivity (H_c), remanent magnetization (M_r), remanence ratio (M_r/M_s), anisotropy constant (K), magnetic moment (η_B), Y–K angle for $CoFe_{2-x}La_xO_4$(x = 0.00, 0.05, 0.10, 0.15, 0.20) nanoparticles

x	D (nm)	a (Å)	M_s(emu/g)	H_c (Oe)	M_r (emu/g)	M_r/M_s	$Kx10^3$(erg/g)	η_B (μ_B)	α_{YK} (deg)
0.00	21	8.3886	53	785	18	0.34	43.34	2.23	0.0
0.05	14	8.3463	36	593	8	0.22	22.24	1.54	0.0
0.10	11	8.3539	30	538	7	0.23	16.81	1.30	18.04
0.15	9	8.3693	26	578	5	0.19	15.65	1.15	28.59
0.20	8	8.3964	16	611	3	0.18	10.18	0.72	47.36

with saturation magnetization, coercivity, and remanence. It can also be observed that the value of saturation magnetization (M_s) decreases with addition of La^{3+} ion in $CoFe_2O_4$ nanoparticles. This can be explained according to Neel's sub-lattice model [43]. According to Neel's sub-lattice model, the magnetic moment per formula unit is given by $\eta_B = M_B - M_A$, where M_B and M_A are the [B] and (A) sub-lattice magnetic moments in μ_B. Generally, rare-earth ions substituted in spinel ferrite occupy octahedral site [B] due to their larger ionic radii. The M_s is decreased with increased substitution of La^{3+} ion in $CoFe_2O_4$ nanoparticles, suggesting the added non-magnetic La^{3+} preferred to octahedral [B] site by displacing Fe^{3+} ions from octahedral site [B] to tetrahedral site (A) by diluting magnetic moment

of the [B] site. The total magnetization of $CoFe_{2-x}La_xO_4$ (x = 0.0, 0.05, 0.10, 0.15, 0.20) nanoparticles is the difference between the magnetization of octahedral [B] and tetrahedral (A) site, and thereby, M_s is reduced with addition of La^{3+} ion. The displacement of Fe^{3+} ions from octahedral site [B] with addition of La^{3+} can be noticed from XPS results as tabulated in Table 4. The magnetic properties of spinel ferrite strongly depend on cation distribution at tetrahedral and octahedral site. Three types of exchange interactions are involved between the magnetic ions at these two site in spinel structure, i.e., AA interaction, BB interaction and AB interaction; in which AB interaction dominates over other two interactions [44]. Furthermore, the substitution of La^{3+} ions in $CoFe_2O_4$ nanoparticles monotonically
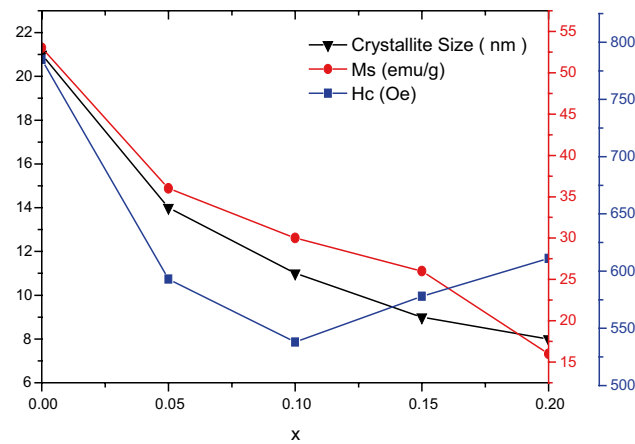
Fig. 6 Dependence of saturation magnetization (M_s), coercivity (H_c), and crystallite size with La ion concentration 'x' in $CoFe_{2-x}La_xO_4$ nanoparticles synthesized by starch-assisted sol–gel combustion method

Fig. 7 Dependence of magnetic moment η_B and Y–K angle (α_{yk}) of $CoFe_{2-x}La_xO_4$ nanoparticles on La concentration 'x'

decreases the value of M_s from 53 emu/g (x = 0.00) to 16 emu/g (x = 0.20) with the decrease of crystallite size 21 nm to 8 nm, as shown in Fig. 6. The decrease in magnetization with crystallite size is associated with surface effect [45]. This surface effect is associated with the existence of a dead magnetic layer due to the surface spin disorder. The number of spins at the surface of $CoFe_{2-x}La_xO_4$ (x = 0.0, 0.05, 0.10, 0.15, 0.20) nanoparticles increases with decrease of crystallite size [46].

The variation of coercivity with increasing La^{3+} ion concentration in cobalt ferrite nanoparticles is tabulated in Table 4 and shown in Fig. 6. It can be notice that the coercivity decreases from 785 Oe (x = 0.0) to 538 Oe (x = 0.10) with addition of La^{3+} ion concentration and then increases on further addition of La^{3+} ion from 538 Oe (x = 0.10) to 611 Oe (x = 0.20). The coercivity of $CoFe_{2-x}La_xO_4$ (x = 0.0, 0.05, 0.10, 0.15, 0.20) nanoparticles depends on magneto crystalline anisotropy constant, cation distribution, strain, defect, and porosity, etc. [38]. The anisotropy constant of $CoFe_{2-x}La_xO_4$ (x = 0.0, 0.05, 0.10, 0.15, 0.20) nanoparticles is estimated using following relation [47]:

$$H_c = \frac{0.96\,K}{M_S}$$

where, K is anisotropy constant.

The magnetic moment (η_B) per unit formula in magnetic moment (μ_B) was evaluated from the following relation [48]:

$$\eta_B = \frac{M \times M_s}{5585}$$

where, M is the molecular weight. The calculated values of magnetic moments and anisotropy constant are tabulated in Table 4. The decrease in the value of magnetic moment
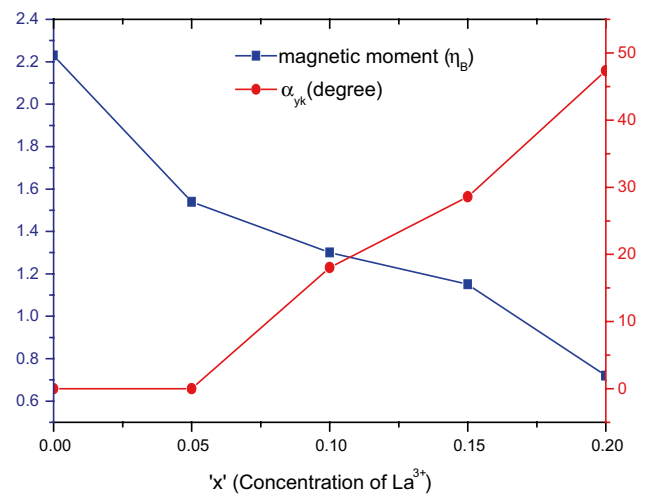
η_B with increase of La^{3+} ions in cobalt ferrite nanoparticles can be explained on the basis of Yafet and Kittel (Y-K) model [49]. According to this model, the B lattice can be divided into two sub-lattices, B_1 and B_2, each sub-lattice has equal magnetic moment in magnitude with oppositely canted at the same angle, α_{y-k}, relative to the net magnetization [50]. The spin canting or non-collinear magnetic order is a behaviour in which spin orientations of magnetic ions aligned with making angles from the preferred direction. The existence of spin canting and the behaviour of magnetic moment with La^{3+} ion substitution can be determined by the Y-K angle [51]. The Yafet-Kittel (Y-K) angles are calculated by using the following relation [52]:

$$\eta_B = (6 + x)Cos\alpha_{yk} - 5(1 - x)$$

where 'x' represents concentration of La^{3+} ion substitution in cobalt ferrite nanoparticles. The calculated value of Y-K angle is tabulated in Table 4. Figure 7 shows the dependence of magnetic moment and Y-K angle of $CoFe_{2-x}La_xO_4$ nanoparticles on the concentration of La^{3+} ion. It can be seen from Table 4 and Fig. 7 that the $\alpha_{yk}=0$ for x = 0.00 and 0.05, which indicates that the magnetization can be explained on the basis of the Neel's two sub-lattice model, i.e., $CoFe_{2-x}La_xO_4$ (x = 0.00 and 0.05) exhibit a Neel's type of magnetic ordering. Furthermore, it can be also notice from Table 4 and Fig. 7 that the value of Y-K angle gradually increases with increase of concentration of La^{3+} ions in cobalt ferrite nanoparticles. The non-zero Y-K angle suggest that the magnetization behaviour cannot be explained on Neel's two lattice model due to presence of non-collinear spin structure on octahedral (B) sites, which increases the B–B interaction and consequently decreases the A–B interaction [53].

3.6 Dielectric property

3.6.1 Dielectric constant

Dielectric spectroscopic study provides information about the crystal structure, grain, grain boundary, charge storage capabilities and transport properties for dielectric material [54]. Figure 8 shows the real (ϵ') and imaginary (ϵ'') part of dielectric constant of $CoFe_{2-x}La_xO_4$(x = 0.00, 0.05, 0.10, 0.15, 0.20) nanoparticles with frequency at room temperature. It is noticeable from Fig. 8 that the synthesized $CoFe_{2-x}La_xO_4$ (x = 0.00, 0.05, 0.10, 0.15, 0.20) nanoparticles exhibit dielectric dispersion where both real (ϵ') and imaginary (ϵ'') part of dielectric constant decreases rapidly at low frequency region, however, it is frequency independent at higher frequency region. The dispersion in dielectric constant is associated with Maxwell–Wagner type of interfacial polarization in agreement with Koop's phenomenological theory [55]. According to this model for inhomogeneous structure as during the synthesis of ferrites in polycrystalline form, the formation of highly conductive grains with thin layers of poorly conducting grain boundaries take place and thereby it behaves as heterogeneous dielectric materials. At low frequency, grain boundaries are more effective and as frequency increases highly conducting grains come in action due to which dielectric constant decreases. B. K. Bammannavar et al. [56] reported that the dielectric dispersion of ferrite is due to the exchange mechanism of charges among the ions situated at crystallographically equivalent sites. It is attributed to polarization due to changes in the valence states of cations and space charge polarizat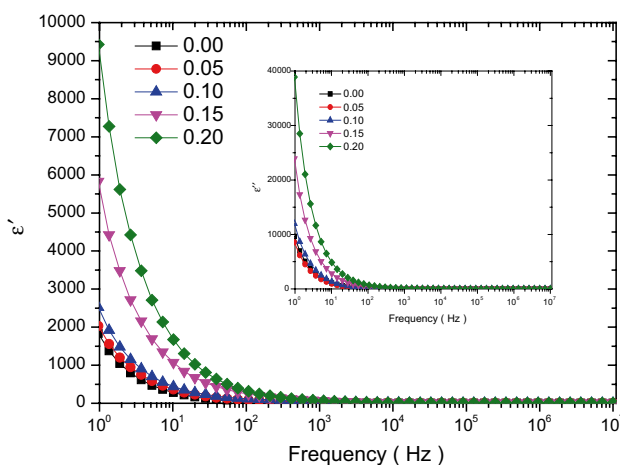ion. At higher frequency, the dielectric constant remains independent of frequency and it is associated with inability of electric dipoles to follow the variation in ac applied electric field.

3.6.2 Dielectric loss

Dielectric loss tangent (tan δ) is dissipation of energy in dielectric material and associated with impurities, defects and imperfections, which cause polarization to lag behind with the applied electric field [57]. Figure 9 shows the dependence of dielectric loss (tanδ) of $CoFe_{2-x}La_xO_4$ (x = 0.00, 0.05, 0.10, 0.15, 0.20) nanoparticles with frequency at room temperature. It is noticeable that the dielectric loss (tanδ) exhibit normal dielectric behaviour for $CoFe_{2-x}La_xO_4$ (x = 0.00, 0.05, 0.10, 0.15, 0.20) nanoparticles. At low frequency dielectric loss decreases with frequency and almost frequency independent at high frequency. The high value of dielectric loss at low frequency is due to high resistivity of grain boundaries which are more effective at low frequencies. Because of high resistivity of grain boundaries more energy is required for electron exchange between Fe^{2+} and Fe^{3+} ions, which relates maximum energy loss. However, at high frequency small energy is sufficient for electron exchange and therefore less energy loss [58]. Further, when the jumping frequency of electron between the Fe^{2+} and Fe^{3+} is equal to frequency of applied field with the condition $\omega\tau = 1$, (where $\omega = 2\pi f_{max}$ and τ is relaxation time), the dielectric loss peak occurred [59], as shown in Fig. 9. In other words, when the hopping frequency of charge carriers matches well with the frequency of applied electric field, the maximum electrical energy is transferred to oscillating ions and consequently due to
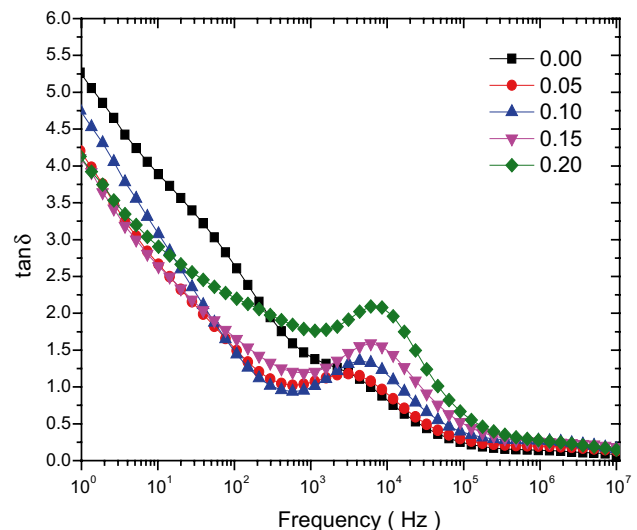

Fig. 8 The dependence of real part of dielectric constant (ϵ') of $CoFe_{2-x}La_xO_4$ (x = 0.00, 0.05, 0.10, 0.15, 0.20) nanoparticles with frequency at room temperature (inset: dependence of imaginary part of dielectric constant (ϵ'') with frequency for $CoFe_{2-x}La_xO_4$ (x = 0.00, 0.05, 0.10, 0.15, 0.20) nanoparticles)

Fig. 9 The dependence of dielectric loss (tanδ) of $CoFe_{2-x}La_xO_4$ (x = 0.00, 0.05, 0.10, 0.15, 0.20) nanoparticles with frequency at room temperature

Table 5 Electrical parameters for CoFe$_{2-x}$La$_x$O$_4$ (x = 0.00, 0.05, 0.10, 0.15, 0.20) nanoparticles: dielectric constant (ϵ' & ϵ''), dielectric loss (tanδ) and AC conductivity (σ_{ac}) at 100 Hz and 1 KHz

x	ϵ'		ϵ''		tanδ		σ (S cm^{-1})	
	At 100 Hz	At 1 kHz	At 100 Hz	At 1 kHz	At 100 Hz	At 1 kHz	At 100 Hz	At 1 kHz
0.00	57	17	145	24	2.60	1.41	8.59×10^{-9}	1.37×10^{-8}
0.05	91	31	127	32	1.50	1.05	7.32×10^{-9}	1.88×10^{-8}
0.10	122	48	179	47	1.47	0.99	1.04×10^{-9}	2.66×10^{-8}
0.15	247	73	416	89	1.67	1.19	2.37×10^{-8}	4.93×10^{-8}
0.20	327	69	727	124	2.22	1.76	4.05×10^{-8}	7.17×10^{-8}

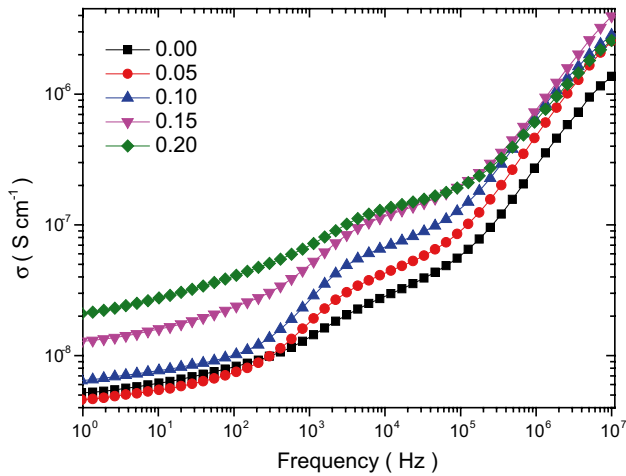**Fig. 10** The dependence of ac conductivity (σ_{ac}) of CoFe$_{2-x}$La$_x$O$_4$ (x = 0.00, 0.05, 0.10, 0.15, 0.20) nanoparticles with frequency at room temperature

Fig. 11 Variation among the dielectric constant, dielectric loss and ac conductivity of CoFe$_{2-x}$La$_x$O$_4$ (x = 0, 0.05, 0.10, 0.15, 0.20) nanoparticles with La ion content 'x'

power loss, a dielectric loss peak occurs. It is also noticeable that the dielectric loss depends on content of doping of La^{3+} ions in cobalt ferrite nanoparticles. The observed value of dielectric loss at 100 Hz and 1 kHz frequency is tabulated in Table 5. It was 2.60 (at 100 Hz) and 1.41 (at 1 kHz) for pure cobalt ferrite nanoparticles, while it was 1.47 (at 100 Hz) and 0.99 (at 1 kHz) for x = 0.10 content of La^{3+} ion in cobalt ferrite nanoparticles. The low value of tanδ at high frequency region indicates that this material has potential for high energy applications.

3.7 AC conductivity

To understand influence of La^{3+} substitution in cobalt ferrite nanoparticles on conduction mechanism, the variation of ac conductivity with frequency is investigated. Figure 10 shows the dependence of ac conductivity (σ_{ac}) of CoFe$_{2-x}$La$_x$O$_4$ (x = 0.00, 0.05, 0.10, 0.15, 0.20) nanoparticles with frequency at room temperature. It is noticeable from Fig. 10 that the electrical conductivity of CoFe$_{2-x}$La$_x$O$_4$ nanoparticles increases slowly at low frequency and rapidly increases at high frequency. In general, the total conductivity is in accordance with following relation [60]:
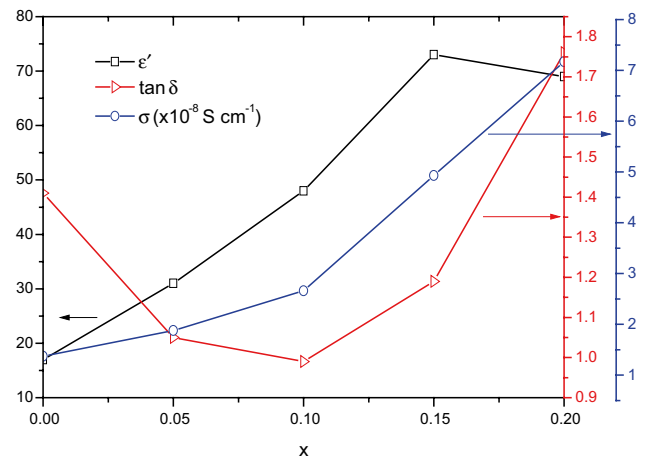
$$\sigma_{tot} = \sigma_o(T) + \sigma(\omega, T) = \sigma_o(T) + B\omega^s$$

where, $\sigma_o(T)$ is dc conductivity due to band conduction and it is frequency independent part, $\sigma(\omega, T)$ is ac conductivity due to hopping process among ions of same element present in more than one valence state. B and s are constants which depends on both temperature and composition; s is a dimensionless quantity having values between 0 and 1, when s = 0 conduction is dc conduction but for s ≤ 1, the conduction is ac conduction. It is well known that in spinel ferrite, the conduction is due to the hopping between ions with mixed valence. In spinel ferrite, the conduction process occurs as a consequence of electron exchange between Fe^{2+} and Fe^{3+} ions and hole exchange between Co^{2+} and Co^{3+} at the octahedral sites [61, 62]. The presence of Fe and Co ions at the octahedral site may cause conduction according to following relation [63–65]:

$$Co^{2+} + Fe^{3+} \leftrightarrow Co^{3+} + Fe^{2+}$$
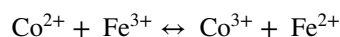
The dependence of ac conductivity of CoFe$_{2-x}$La$_x$O$_4$ nanoparticles on frequency can be explained on the basis of Maxwell–Wagner double layer model for dielectrics [66, 67]. According to this model, at low frequency the resistive grain boundaries are more active and therefore,

the hopping of charge carriers between $Fe^{2+} \leftrightarrow Fe^{3+}$ and $Co^{3+} \leftrightarrow Co^{2+}$ is very much hindered at low frequency and therefore a constant plateau region is noticed. However, at high frequency the conductive grains are more active and therefore support the hopping of charge carriers between neighbouring ions [68]. Furthermore, it is noticeable that the doping of La^{3+} ion in $CoFe_2O_4$ nanoparticles enhances the ac conductivity and also supports the mechanism for the enhancement in the dielectric constant. The value of ac conductivity at frequency 100 Hz and 1 kHz is tabulated in Table 5. It was 8.59×10^{-9} S cm^{-1} (at 100 Hz) and 1.37×10^{-8} S cm^{-1} (at 1 kHz) for pure cobalt ferrite, while it was 4.05×10^{-8} S cm^{-1} (at 100 Hz) and 7.17×10^{-8} S cm^{-1} (at 1 kHz) for x = 0.20 La^{3+} doped cobalt ferrite nanoparticles (Fig.11).

3.8 Modulus and impedance spectroscopy

The modulus and complex impedance spectroscopy is powerful technique to investigate the contribution of the relaxation process of different micro-regions in the polycrystalline materials such as grain, grain boundary and electrode interface [69]. In the present work, the modulus and impedance spectroscopy are used to investigate the effects of grains and grain boundaries because both of them have different relaxation time. The dependence of real part of impedance (Z′) and real part of modulus (M′) of $CoFe_{2-x}La_xO_4$ (x = 0.00, 0.05, 0.10, 0.15, 0.20) nanoparticles with frequency at room temperature is shown in Fig. 12. It can be observed from Fig. 12 that synthesized $CoFe_{2-x}La_xO_4$ (x = 0.00, 0.05, 0.10, 0.15, 0.20)

nanoparticles have low value of M′ at low frequency, which indicates that there is lack of force that governs the mobility of charge carriers under the influence of applied electric field at low frequency. It is also noticeable that M′ tends to zero at low frequency, which indicate negligible or absent electrode polarization phenomenon [70]. Moreover, it is obvious from Fig. 12 that the value of M′ for $CoFe_{2-x}La_xO_4$ (x = 0.00, 0.05, 0.10, 0.15, 0.20) nanoparticles increases with increase of frequency. Furthermore, decrease in resistance (Z′) with increase in frequency for $CoFe_{2-x}La_xO_4$ (x = 0.00, 0.05, 0.10, 0.15, 0.20) nanoparticles can be observed from Fig. 12, which indicate conduction is promoted by applied electric field [71].

The variation of imaginary part of impedance (Z″) and imaginary part of modulus (M″) of $CoFe_{2-x}La_xO_4$ (x = 0.00, 0.05, 0.10, 0.15, 0.20) nanoparticles with frequency at room temperature, is shown in Fig. 13. The electric modulus is associated with the relaxation of electric field in the material when the electric displacement remains constant [72]. The peak in modulus (M″) spectra represents real dielectric relaxation process [73]. The existence of two relaxation peaks in M″ versus frequency plots, as shown in Fig. 13, confirms the presence of both grain and grain boundary effects in spinel ferrite nanoparticles. In the modulus (M″) spectra, the relaxation peak at low frequency side is due to grain boundaries effect and the one at high frequency is contributed by grains effect. Further, the shift in peak position in the imaginary part of modulus (M″) spectra with La^{3+} content in cobalt ferrite nanoparticles can also be notice from Fig. 13. This shift in peak position is associated with dependence of relaxation and correlation between mobile ion charges. The frequency region below
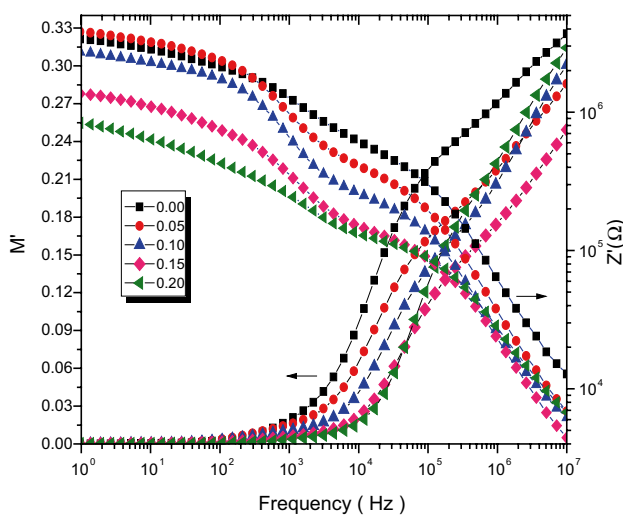

Fig. 12 The dependence of real part of impedance (Z′) and real part of modulus (M′) of $CoFe_{2-x}La_xO_4$ (x = 0.00, 0.05, 0.10, 0.15, 0.20) nanoparticles with frequency at room temperature

Fig. 13 The dependence of imaginary part of impedance (Z″) and imaginary part of modulus (M″) of $CoFe_{2-x}La_xO_4$ (x = 0.00, 0.05, 0.10, 0.15, 0.20) nanoparticles with frequency at room temperature

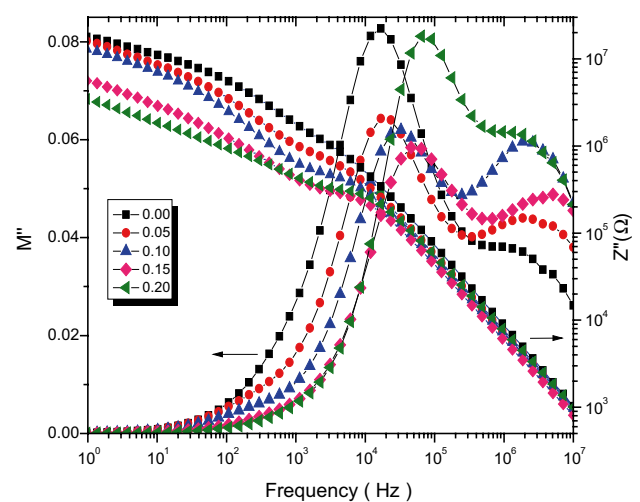the peak in imaginary part of modulus (M″) spectra for $CoFe_{2-x}La_xO_4$ (x = 0.00, 0.05, 0.10, 0.15, 0.20) nanoparticles, indicates the range in which the charge carriers are mobile over long distances, whereas the frequency region above the peak represents the range in which the charge carriers are confined to their potential well, and therefore, localized motion inside the well [74]. The region of existence of peak is associated with transition from long-range to short range mobility with increase of frequency. The existence of peaks in the modulus (M″) spectra indicates conductivity relaxation. The broadening of peak indicates the relaxation with a relaxation constant distribution [75]. Further, the asymmetric broadening of peaks in imaginary part of modulus (M″) spectra for $CoFe_{2-x}La_xO_4$ (x = 0.00, 0.05, 0.10, 0.15, 0.20) nanoparticles, indicates that the conduction mechanism is of non-Debye type [76]. Furthermore, it is also obvious from Fig. 13 that the reactance (Z″) decreases with increase of frequency, which indicates that the conduction is promoted by applied ac electric field. It is also noticeable that the imaginary part of impedance (Z″) spectra tend to merge above 1 kHz frequency, which indicate a possible release of the space charge.
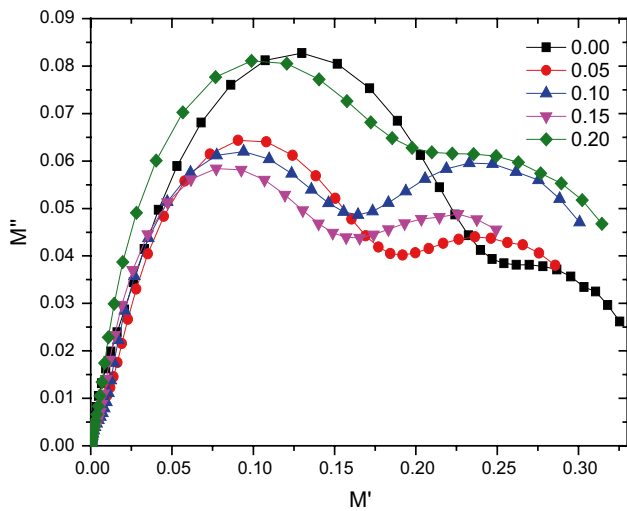

Fig. 14 The cole–cole plot (M′ vs. M″) for $CoFe_{2-x}La_xO_4$ (x = 0.00, 0.05, 0.10, 0.15, 0.20) nanoparticles

The cole–cole plot (M′ vs. M″) for $CoFe_{2-x}La_xO_4$ (x = 0.00, 0.05, 0.10, 0.15, 0.20) nanoparticles is shown in Fig. 14. It is well known that the cole–cole plot of modulus formalism (M′ vs. M″) is more effective than impedance formalism (Z′ vs. Z″) for precisely separating the relaxation effects from grain and grain boundary in nanostructured spinel ferrite material. It is due to imaginary part of impedance (Z″) represents the relaxation dynamics from largest resistance of the material, whereas, imaginary part of the modulus (M″) represents the smallest capacitance (i.e., the highly conductive part) of the material [77]. It is obvious from Fig. 14 that the cole–cole (M′ vs. M″) plots for $CoFe_{2-x}La_xO_4$ (x = 0.00, 0.05, 0.10, 0.15, 0.20) nanoparticles exhibit two semi-circular peaks, which indicates the presence of two type of relaxation phenomenon with different relaxation time (τ), associated with each relaxation. It is associated with electrical heterogeneity in the synthesized $CoFe_{2-x}La_xO_4$ (x = 0.00, 0.05, 0.10, 0.15, 0.20) nanoparticles. The relaxation time, τ, associated with frequency maximum in the modulus spectra, can be evaluated by following relation [78]:

$$\tau = \frac{1}{2\pi f_{M''}}$$

The peak height in M″ versus frequency plot is inversely proportional to the capacitance. Hence, the capacitance values can be calculated at the maximum frequency (f_{max}) using the following relation [79]:

$$C = \frac{\epsilon_o}{2M''_{max}}$$

Further, the resistance values at the maximum frequency (f_{max}) are related by following relation [80]:

$$R = (1/2\pi f_{max} C)$$

The evaluated electrical parameters R_g, C_g and τ_g corresponding to the resistance, capacitance, and the relaxation time of the grain and further R_{gb}, C_{gb} and τ_{gb} corresponding parameters for grain boundary are tabulated in Table 6. The dependence of these electrical parameters on La^{3+} ion in cobalt ferrite nanoparticles can be noticed from the Table 6. It was associated with variation of crystallite

Table 6 Electrical parameters: grain relaxation time (τ_g), grain boundary relaxation time (τ_{gb}), grain resistance (R_g), grain boundary resistance (R_{gb}), grain capacitance (C_g) and grain boundary capacitance (C_{gb}) for $CoFe_{2-x}La_xO_4$ (x = 0.00, 0.05, 0.10, 0.15, 0.20) nanoparticles

x	τ_g (s)	τ_{gb} (s)	R_g (Ω)	R_{gb} (Ω)	C_g (pF)	C_{gb} (pF)
0.00	1.13×10^{-7}	9.29×10^{-6}	9.63×10^2	1.74×10^5	117.82	52.37
0.05	8.23×10^{-8}	9.00×10^{-6}	8.26×10^2	1.31×10^5	99.55	68.68
0.10	8.23×10^{-8}	4.89×10^{-6}	1.11×10^3	6.85×10^4	74.08	71.45
0.15	2.97×10^{-8}	3.25×10^{-6}	3.27×10^2	4.26×10^4	90.78	76.38
0.20	8.49×10^{-8}	2.43×10^{-6}	1.17×10^3	4.44×10^4	72.62	54.69

size and cation distribution with substitution of La^{3+} ion in cobalt ferrite nanoparticles. Furthermore, Fig. 15 shows the modulus plots scaling behaviour (M''/M_{max}'') of $CoFe_{2-x}La_xO_4$ ($x = 0.00, 0.05, 0.10, 0.15, 0.20$) nanoparticles with frequency. The mismatch among the curves with variation in La^{3+} content in cobalt ferrite nanoparticles can be noticed from Fig. 15, which indicate variation in conduction mechanism and relaxation process with variation in grain, grain boundary, crystallite size, cation redistribution in synthesized $CoFe_{2-x}La_xO_4$ ($x = 0.00, 0.05, 0.10, 0.15, 0.20$) nanoparticles by starch-assisted sol–gel self-combustion method.

4 Conclusion

We have successfully synthesized single phase cubic spinel structure of $CoFe_{2-x}La_xO_4$ ($x = 0.00, 0.05, 0.10, 0.15, 0.20$) nanoparticles using a starch-assisted sol–gel self-combustion method. The doping of La^{3+} ions for Fe^{3+} in $CoFe_2O_4$ nanoparticles reduces the crystallite size and influences the cation distribution and consequently influence in the structural, magnetic, dielectric and electrical properties. The variation in magnetic parameters such as saturation magnetization and coercivity with La^{3+} substitution was observed. Cation redistribution in synthesized spinel ferrite nanoparticles was noticed by X-ray photoelectron spectroscopy. The frequency dependent dielectric constant and ac conductivity increases with La ion substitution in cobalt ferrite nanoparticles. Modulus Spectroscopy, which is well developed characterization technique to distinguish grain and gr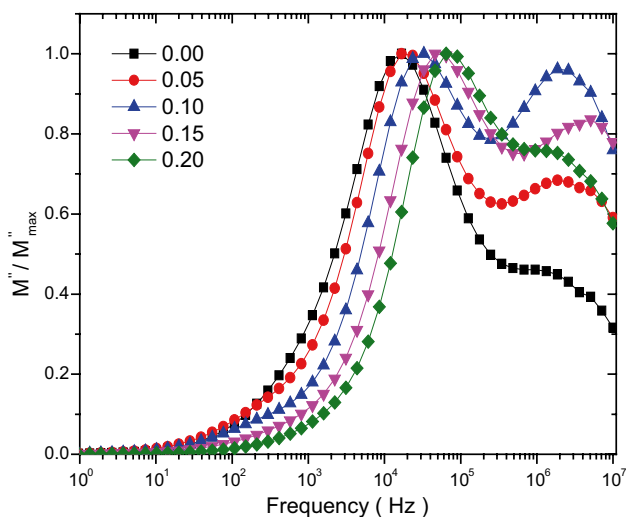ain boundary contribution to the total conductivity, was utilized to evaluate electrical responses of synthesized La^{3+} doped spinel ferrite nanoparticles. Further, the modulus spectra revealed the variation of resistance in terms of grain and grain boundary contributions.

Fig. 15 The modulus plots scaling behaviour (M''/M'_{max}) of $CoFe_{2-x}La_xO_4$ ($x = 0.00, 0.05, 0.10, 0.15, 0.20$) nanoparticles with frequency

References

1. V.J. Sawant, S.R. Bamane, R.V. Shejwal, S.B. Patil, Comparison of drug delivery potentials of surface functionalized cobalt and zinc ferrite nanohybrids for curcumin in to MCF-7 breast cancer cells. J. Magn. Magn. Mater. **417**, 222–229 (2016)
2. J. Xie, C. Yan, Y. Yan, L. Chen, L. Song, Z. Fengchao, Y. An, G.J. Teng, N. Gu, Y. Zhang, Multi-modal Mn-Zn ferrite nanocrystals for magnetically-induced cancer targeted hyperthermia: a comparison of passive and active targeting effects. Nanoscale (2016). Doi:10.1039/C6NR03916B
3. W. Zhang, X. Zuo, C.D. Zhang, Wu and S Ravi P Silva, Cr^{3+} substituted spinel ferrite nanoparticles with high coercivity. Nanotechnology **27**, 245707 (2016)
4. A. Poorbafrani, E. Kiani, Enhanced microwave absorption properties in cobalt–zinc ferrite based nanocomposites. J. Magn. Magn. Mater. **416**, 10–14 (2016)
5. C. Sujatha, K. Venugopal Reddy, K. Sowri Babu, A. RamaChandra Reddy, M. Buchi Suresh, K.H. Rao, Effect of Mg substitution on electromagnetic properties of NiCuZn ferrite. J. Magn. Magn. Mater. **340**, 38–45 (2013)
6. P. Samoila, C. Cojocaru, L. Sacarescu, P.P. Dorneanu, A.A. Domocos, A. Rotaru, Remarkable catalytic properties of rare-earth doped nickel ferrites synthesized by sol-gel auto-combustion with maleic acid as fuel for CWPO of dyes. Appl. Catal. B **202**, 21–32 (2017)
7. Y. Cao, H. Qin, X. Niu, D. Jia, Simple solid-state chemical synthesis and gas-sensing properties of spinel ferrite materials with different morphologies. Ceram. Int. 42 (2016) 10697–10703.
8. J. Mao, X. Hou, F. Huang, K. Shen, K.H. Lam, Q Ru, S Hu, Zn substitution NiFe2O4 nanoparticles with enhanced conductivity as high-performances electrodes for lithium ion batteries. J. Alloys Compd. **676**, 265–274 (2016)
9. V. Mameli, A. Musinu, A. Ardu, G. Ennas, D. Peddis, D. Niznansky, C. Sangregorio, C. Innocenti, N.T.K. Thanh, C. Cannas, Studying the effect of Zn-substitution on the magnetic and hyperthermic properties of cobalt ferrite nanoparticles. Nanoscale **8**, 10124–10137 (2016)
10. G. Datt, M.S. Bishwas, R.M. M., A.C. Abhyankar, Observation of magnetic anomalies in one-step solvothermally synthesized nickel-cobalt ferrite nanoparticles. Nanoscale **8**, 5200–5213 (2016)
11. S. Jauhar, J. Kaur, A. Goyal, S. Singhal, Tuning the properties of cobalt ferrite: a road towards diverse applications. RSC Adv. **6**, 97694–97719 (2016)
12. A Goyal, S. Kapoor, P. Samuel, V. Kumar, S. Singhal, Facile protocol for reduction of nitroarenes using magnetically recoverable $CoM_{0.2}Fe_{1.8}O_4$ (M = Co, Ni, Cu and Zn) ferrite nanocatalysts. RSC Adv. 5, 51347–51363 (2015)
13. V. Postica, J. Grottrup, R. Adelung, O. Lupan, A.K. Mishra, N.H. de Leeuw, N. Ababii, J.F.C. Carreira, J. Rodrigues, N.B. Sedrine, M.R. Correia, T. Monteiro, V. Sontea, Y.K. Mishra,

Multifunctional materials: a case study of the effects of metal doping on ZnO tetrapods with bismuth and tin oxides. Adv. Funct. Mater. **27**, 1604676 (2017)

14. J. Gröttrup, I. Paulowicz, A. Schuchardt, V. Kaidas, S. Kaps, O. Lupan, R. Adelung, Y. K. Mishra, Three-dimensional flexible ceramics based on interconnected network of highly porous pure and metal alloyed ZnO tetrapods. Ceram. Int. **42**, 8664–8676 (2016)

15. M. Najim, G. Modi, Y.K. Mishra, R. Adelung, D. Singh, V. Agarwala, Ultra-wide bandwidth with enhanced microwave absorption of electroless Ni-P coated tetrapod-shaped ZnO nano- and microstructures. Phys. Chem. Chem. Phys. **17**, 22923–22933 (2015)

16. Y.K. Mishra, S. Kaps, A. Schuchardt, I. Paulowicz, X. Jin, D. Gedamu, S. Freitag, M. Claus, S. Wille, A. Kovalev, S.N. Gorb, R. Adelung, Fabrication of macroscopically flexible and highly porous 3D semiconductor networks from interpenetrating nanostructures by a simple flame transport approach. Part. Part. Syst. Charact. **30**, 775–783 (2013)

17. B.P. Jacob, S. Thankachan, S. Xavier, E.M. Mohammed, Effect of Tb^{3+} substitution on structural, electrical and magnetic properties of sol–gel synthesized nanocrystalline nickel ferrite. J. Alloys Compd. **578**, 314–319 (2013)

18. Z. Liua, Z. Penga, C. Lva, X. Fub, Doping effect of Sm^{3+} on magnetic and dielectric properties of Ni-Zn ferrites, Ceram. Int. **43**, 1449–1454 (2017)

19. K.S. Lohar, A.M. Pachpinde, M.M. Langade, R.H. Kadam, E. Sagar, Shirsath, self-propagating high temperature synthesis, structural morphology and magnetic interactions in rare earth Ho^{3+} doped $CoFe_2O_4$ nanoparticles. J. Alloys Compd. **604**, 204–210 (2014)

20. X Wu, W. Wang, N. Song, X. Yang, S. Khaimanov, N. Tsidaeva, From nanosphere to nanorod: tuning morphology, structure and performance of cobalt ferrites via Pr^{3+} doping. Chem. Eng. J. **306**, 382–392 (2016)

21. N. Sharma, P. Aghamkar, S. Kumar, M. Bansal, R.P. Anju, Tondon, Study of structural and magnetic properties of Nd doped zinc ferrites. J. Magn. Magn. Mater. **369**, 162–167 (2014)

22. H.Z. Duan, F.L. Zhou, X. Cheng, G.H. Chen, Q.L. Li, Preparation of hollow microspheres of Ce^{3+} doped NiCo ferrite with high microwave absorbing performance. J. Magn. Magn. Mater. **424**, 467–471 (2017)

23. P. Samoila, L. Sacarescu, A.I. Borhan, D. Timpu, M. Grigoras, N. Lupu, M. Zaltariov, V. Harabagiu, Magnetic properties of nanosized Gd doped Ni–Mn–Cr ferrites prepared using the sol–gel autocombustion technique. J. Magn. Magn. Mater. **378**, 92–97 (2015)

24. R.C. Kambale, K.M. Song, Y.S. Koo, N. Hur, Low temperature synthesis of nanocrystalline Dy^{3+} doped cobalt ferrite: structural and magnetic properties. J. Appl. Phys **110**, 053910 (2011)

25. R. Indhrajothi, I. Prakash, M. Venkateswarlu, N. Satyanarayana, Lanthanum ion (La^{3+}) substituted $CoFe_2O_4$ anode material for lithium ion battery applications. New J. Chem. **39**, 4601–4610 (2015)

26. S.F. Mansour, O.M. Hemeda, S.I. El-Dek, B.I. Salem, Influence of La doping and synthesis method on the properties of $CoFe_2O_4$ nanocrystals. J. Magn. Magn. Mater. **420**, 7–188 (2016)

27. L. Kumar, M. Kar, Effect of La^{3+} substitution on the structural and magnetocrystalline anisotropy of nanocrystalline cobalt ferrite ($CoFe_{2-x}La_xO_4$). Ceram. Int. **38**, 4771–4782 (2012)

28. P. Kumar, S.K. Sharma, M. Knobel, M. Singh, Effect of La^{3+} doping on the electric, dielectric and magnetic properties of cobalt ferrite processed by co-precipitation technique. J. Alloys Compd. **508**, 115–118 (2010)

29. K. Kamala Bharathi, R.J. Tackett, C.E. Botez, C.V. Ramana, Coexistence of spin glass behavior and long-range ferromagnetic ordering in La- and Dy-doped Co ferrite. J. Appl. Phys **109**, 07A510 (2011)

30. Z.Z. Lazarevic, C. Jovalekic, A. Milutinovic, D. Sekulic, V.N. Ivanovski, A. Recnik, B. Cekic, N.Z. Romcevic, Nanodimensional spinel $NiFe_2O_4$ and $ZnFe_2O_4$ ferrites prepared by soft mechanochemical synthesis. J. Appl. Phys. **113**, 187221 (2013)

31. P. Thakur, R. Sharma, M. Kumar, S. C. Katyal, N. S. Negi, N. Thakur, V. Sharma, P. Sharma, Superparamagnetic La doped Mn–Zn nano ferrites: dependence on dopant content and crystallite size. Mater. Res. Express **3**, 075001 (2016)

32. A. Sattar, A. M. Samy, R. S. El-Ezza, A. E. Eatah, Effect of rare earth substitution on magnetic and electrical properties of Mn–Zn ferrites. Phys. Status Solidi (a). **193**(1), 86–93 (2002).

33. A. Murugesan, G. Chandrasekaran, Impact of Gd^{3+} substitution on the structural, magnetic and electrical properties of cobalt ferrite nanoparticles, RSC Adv. **5** 73714–73725 (2015)

34. S.F. Mansour, O.M. Hemeda, S.I. El-Dek, B.I. Salem, Influence of La doping and synthesis method on the properties of $CoFe_2O_4$ nanocrystals. J. Magn. Magn. Mater. **420**, 7–18 (2016)

35. C. Singh, A. Goyal, S. Singhal, Nickel-doped cobalt ferrite nanoparticles: efficient catalysts for the reduction of nitroaromatic compounds and photo-oxidative degradation of toxic dyes. Nanoscale **6**, 7959–7970 (2014)

36. V. Jagadeesha Angadi, B. Rudraswamy, K. Sadhana, S. Ramana Murthy, K. Praveena, Effect of Sm^{3+}-Gd^{3+} on structural, electrical and magnetic properties of Mn-Zn ferrites synthesized via combustion route. J. Alloys Compd. **656**, 5–12 (2016)

37. S. G. Kakade, R. C. Kambale, C. V. Ramanna, Y. D. Kolekar, Crystal strain, chemical bonding, magnetic and magnetostrictive properties of erbium (Er^{3+}) ion substituted cobalt-rich ferrite ($Co_{1.1}Fe_{1.9-x}Er_xO_4$). RSC Adv. **6**, 33308–33317 (2016)

38. S. Joshi, M. Kumar, S. Chhoker, A. Kumar, M. Singh, Effect of Gd^{3+} substitution on structural, magnetic, dielectric and optical properties of nanocrystalline $CoFe_2O_4$. J. Magn. Magn. Mater. **426**, 252–263 (2017)

39. S. Thota, S.C. Kashyap, S.K. Sharma, V.R. Reddy, Cation distribution in Ni-substituted $Mn_{0.5}Zn_{0.5}Fe_2O_4$ nanoparticles: A Raman, Mössbauer, X-ray diffraction and electron spectroscopy study. Mater. Sci. Eng. B. **206**, 69–78 (2016)

40. A.V. Humbe, A.C. Nawle, A.B. Shinde, K.M, Jadhav, Impact of Jahn Teller ion on magnetic and semiconducting behaviour of Ni-Zn spinel ferrite synthesized by nitrate-citrate route. J. Alloys Compd. **691**, 343–354 (2017)

41. G. Wang, Y Ma, Z. Wei, M Qi, Development of multifunctional cobalt ferrite/graphene oxide nanocomposites for magnetic resonance imaging and controlled drug delivery. Chem. Eng. J. **289**, 150–160 (2016)

42. Kalpana Panwar, Shailja Tiwari, Komal Bapna, N.L. Heda, R.J. Choudhary, D.M. Phase, B.L. Ahuja, The effect of Cr substitution on the structural, electronic and magnetic properties of pulsed laser deposited $NiFe_2O_4$ thin films. J. Magn. Magn. Mater. **421**, 25–30 (2017)

43. S.K. Gore, R.S. Mane, M. Naushad, S.S. Jadhav, M.K. Zate, Z.A. Alothman, B.K. Hui, Influence of Bi^{3+}-doping on the magnetic and Mössbauer properties of spinel cobalt ferrite. Dalton Trans. **44**, 6384–6390 (2015).

44. H.S. Aziz, S. Rasheed, R.A. Khan, A. Rahim, J. Nisar, S.M. Shah, F. Iqbal, A.R. Khan, Evaluation of electrical, dielectric and magnetic characteristics of Al–La doped nickel spinel ferrites. RSC Adv. **6**, 6589–6597 (2016)

45. Z.K. Karakas, R. Boncukcuoglu, I.H. Karakas, The effects of heat treatment on the synthesis of nickel ferrite ($NiFe_2O_4$) nanoparticles using the microwave assisted combustion method. J. Magn. Magn. Mater. **374**, 298–306 (2015)

46. C. Murugesan, G. Chandrasekaran, Impact of Gd^{3+} substitution on the structural, magnetic and electrical properties of cobalt ferrite nanoparticles. RSC Adv. **5**, 73714–73725 (2015)

47. R. C. Kambale, P. A. Shaikh, S. S. Kamble, Y. D. Kolekar, Effect of cobalt substitution on structural, magnetic and electric properties of nickel ferrite. J. Alloy Comp. **478**, 599–603 (2009)

48. D. S. Nikam, S.V. Jadhav, V.M. Khot, R.A. Bohara, C.K. Hong, S.S. Mali, S.H. Pawar, Cation distribution, structural, morphological and magnetic properties of $Co_{1-x}Zn_xFe_2O_4$ (x = 0–1) nanoparticles, RSC Adv. **5**, 2338 (2015)

49. Y. Yafet, C. Kittel, Antiferromagnetic arrangements in ferrites. Phys. Rev **87**(2), 290–294 (1952)

50. D.S. Nikam, S.V. Jadhav, V.M. Khot, R.A. Bohara, C.K. Hong, S.S. Mali, S.H. Pawar, Cation distribution, structural, morphological and magnetic properties of $Co_{1-x}Zn_xFe_2O_4$ (x = 0–1) nanoparticles. RSC Adv. **5**, 2338–2345 (2015)

51. R.S. Yadav, J. Havlica, J. Masilko, L. Kalina, J. Wasserbauer, M. Hajdúchová, V. Enev, I. Kuřitka, Z. Kožáková, Impact of Nd^{3+} in $CoFe_2O_4$ spinel ferrite nanoparticles on cation distribution, structural and magnetic properties. J. Magn. Magn. Mater. **399**, 109–117 (2016)

52. M.U. Rana, M. Ul-Islam, I. Ahmad, T. Abbas, Determination of magnetic properties and Y—K angles in Cu—Zn—Fe—O system. J. Magn. Magn. Mater. **187**, 242–246 (1998)

53. M. Ajmal, A. Maqsood, Structural, electrical and magnetic properties of $Cu_{1-x}ZnxFe_2O_4$ ferrites (0 ≤ x ≤ 1). J. Alloys Compd. **460**, 54–59 (2008)

54. A. Chandran, K.C. George, Defect induced modifications in the optical, dielectric, and transport properties of hydrothermally prepared ZnS nanoparticles and nanorods, J Nanopart Res **16**, 2238 (2014)

55. M.D. Rahaman, M.D. Mia, M.N.I. Khan, A.K.M. Akther Hossain, Study the effect of sintering temperature on structural, microstructural and electromagnetic properties of 10% Ca-doped $Mn_{0.6}Zn_{0.4}Fe_2O_4$. J. Magn. Magn. Mater. **404**, 238–249 (2016)

56. B.K. Bammannavar, L.R. Naik, Electrical properties and magnetoelectric effect in $(x)Ni_{0.5}Zn_{0.5}Fe_2O_4$ + $(1–x)$BPZT composites, Smart Mater. Struct. **18**, 085013 (2009)

57. M. Amin, H.M. Rafique, M. Yousaf, S.M. Ramay, S. Atiq, Structural and impedance spectroscopic analysis of Sr/Mn modified $BiFeO_3$ multiferroics, J Mater Sci **27**, 11003–11011 (2016)

58. R. Ahmad, I.H. Gul, M. Zarrar, H. Anwar, M.B. Niazi, A. Khan, Improved electrical properties of cadmium substituted cobalt ferrites nano-particles for microwave application. J. Magn. Magn. Mater. **405**, 28–35 (2016)

59. D.M. Jnaneshwara, D.N. Avadhani, B. Daruka Prasad, H. Nagabhushana, B.M. Nagabhushana, S.C. Sharma, S.C. Prashantha, C. Shivakumara, Role of Cu^{2+} ions substitution in magnetic and conductivity behaviour of nano-$CoFe_2O_4$. Spectrochim. Acta Part A. **132**, 256–262 (2014)

60. N. Kumari, V. Kumar, S.K. Singh, Structural, dielectric and magnetic investigations on Al^{3+} substituted Zn-ferrospinels, RSC Adv. **5**, 37925 (2015)

61. M. Hashim, R.K. Alimuddin, S.E. Shirsath, R.K. Kotnala, S.S. Meena, S. Kumar, A. Roy, R.B. Jotania, P. Bhatt, R. Kumar, Influence of Ni^{2+} substitution on the structural, dielectric and magnetic properties of Cu–Cd ferrite nanoparticles. J. Alloys Compd. **573**, 198–204 (2013)

62. H.S. Aziz, S. Rasheed, R.A. Khan, A. Rahim, J. Nisar, S.M. Shah, F. Iqbal, A.R. Khan, Evaluation of electrical, dielectric and magnetic characteristics of Al–La doped nickel spinel ferrites, RSC Adv. **6**, 6589–6597 (2016)

63. M.J. Iqbal, R.A. Khan, S. Mizukami, T. Miyazaki, Mossbauer, magnetic and microwave absorption characteristics of substituted W-type hexaferrites nanoparticles. Ceram. Int. **38**, 4097–4103 (2012)

64. S.M. Patange, S.E. Shirsath, K.S. Lohar, S.S. Jadhav, N. Kulkarni, K.M. Jadhav, Electrical and switching properties of $NiAl_xFe_{2x}O_4$ ferrites synthesized by chemical method. Phys. B. **406**, 663–668 (2011)

65. S. Verma, J. Chand, M. Singh, Structural and electrical properties of Al^{3+} ions doped nanocrystalline $Mg_{0.2}Mn_{0.5}Ni_{0.3}Al_yFe_{2y}O_4$ ferrites synthesized by citrate precursor method. J. Alloy. Compd. **587**, 763–770 (2014)

66. M A Ahmed, S F Mansour, M A Abdo, Electrical properties of Cu substituted Co nano ferrite. Phys. Scr. **86**, 025705 (2012)

67. R. S. Yadav, J. Havlica, J. Masilko, J. Tkacz, I. Kuritka, J. Vilcakova, Anneal-tuned structural, dielectric and electrical properties of $ZnFe_2O_4$ nanoparticles synthesized by starch-assisted sol–gel auto-combustion method, J Mater Sci **27**, 5992–6002 (2016)

68. S.K. Mandal, S. Singh, P. Dey, J.N. Roy, P.R. Mandal, T.K. Nath, Frequency and temperature dependence of dielectric and electrical properties of TFe_2O_4 (T = Ni, Zn, $Zn_{0.5}Ni_{0.5}$) ferrite nanocrystals. J. Alloys Compd. **656**, 887–896 (2016)

69. Y. Pu, Z. Dong, P. Zhang, Y. Wu, J. Zhao, Y. Luo, Dielectric, complex impedance and electrical conductivity studies of the multiferroic $Sr_2FeSi_2O_7$-crystallized glass-ceramics. J. Alloys Compd. **672**, 64–71 (2016)

70. A. Tabib, N. Sdiri, H. Elhouichet, M. Férid, Investigations on electrical conductivity and dielectric properties of Na doped ZnO synthesized from sol gel method, J. Alloys Compd. **622**, 687–694 (2015)

71. M.M. Costa, G.F.M. Pires, Jr., A.J. Terezo, M.P.F. Grac, A.S.B. Sombra, Impedance and modulus studies of magnetic ceramic oxide $Ba_2Co_2Fe_{12}O_{22}$ (Co_2Y) doped with Bi_2O_3. J. Appl. Phys. **110**, 034107 (2011)

72. D.K. Pradhan, P. Misra, V.S. Puli, S. Sahoo, D.K. Pradhan, S.R. Katiyar, Studies on structural, dielectric, and transport properties of $Ni_{0.65}Zn_{0.35}Fe_2O_4$. J. Appl. Phys **115**, 243904 (2014)

73. N. Ortega, Ashok Kumar, P. Bhattacharya, S.B. Majumder, R.S. Katiyar, Impedance spectroscopy of multiferroic $PbZr_xTi_{1-x}O_3$/$CoFe_2O_4$ layered thin films. Phys. Rev. B **77**, 014111 (2008)

74. S. Nasri, A. Oueslati, I. Chaabane, M. Gargouri, AC conductivity, electric modulus analysis and electrical conduction mechanism of $RbFeP_2O_7$ ceramic compound. Ceram. Int. **42**, 14041–14048 (2016)

75. M.M. Costa, G.F.M. Pires Jr., A.J. Terezo, M.P.F. Grac, A.S.B. Sombra, Impedance and modulus studies of magnetic ceramic oxide $Ba_2Co_2Fe_{12}O_{22}(Co_2Y)$ doped with Bi_2O_3. J. Appl. Phys **110**, 034107 (2011)

76. R.K. Panda, R. Muduli, S.K. Kar, D. Behera, Investigation of electric transport behavior of bulk $CoFe_2O_4$ by complex impedance spectroscopy. J. Alloys Compd. **587**, 481–486 (2014)

77. R.N. Bhowmik, I.P. Muthuselvam, Dielectric properties of magnetic grains in $CoFe_{1.95}Ho_{0.05}O_4$ spinel ferrite. J. Magn. Magn. Mater. **335**, 64–74 (2013)

78. S. Narayanan, A.K. Baral, V. Thangadurai, Dielectric characteristics of fast Li ion conducting garnet-type $Li_{5+2x}La_3Nb_{2-x}Y_xO_{12}$ (x = 0. 25, 0.5 and 0.75)., Phys. Chem. Chem. Phys. DOI:10.1039/c6cp02287a

79. K. Rasool, M.A. Rafiq, M. Ahmad, Z. Imran, M.M. Hasan, TiO_2 nanoparticles and silicon nanowires hybrid device: Role of interface on electrical, dielectric, and photodetection properties. Appl. Phys. Lett. **101**, 253104 (2012)

80. D.C. Sinclair, A.R. West, Impedance and modulus spectroscopy of semiconducting $BaTiO_3$ showing positive temperature coefficient of resistance. J. Appl. Phys **66**(8), 3850–3856 (1989)